[5]Landau, L.D. and Lifshits, E.M. Hydrodynamics, Moscow: Nauka, 1986, 736 pp (in Russian).

[6]Grudnitsky, V.G., Prokhorchuk, Yu.A., and Rybak S.P., "Calculation of the irregular stage of diffraction of a shock wave on a blund body," Zh.vych. Mat. Mat. Fiz., 1978, Vol. 18, No. 3, pp 789-795.

[7]Godunov, S.K., Zabrodin, A.V. et al., Numerical Solution of Multidimensional Problems in Gas Dynamics, Moscow: Nauka, 1976, 400 pp (in Russian).

[8]Zaslavsky, B.I., Morozkin, S.Yu., Shlegel, V.R., and Shcherbin, M.D., "The shock wave motion along a hard surface covered with a light gas layer," (deposited at VINITI, No. 39, 65-V87 Dep.).

Turbulent Wall Jet in a Mach Reflection Flow

A. L. Kuhl*
R & D Associates, Los Angeles, California
and
R. E. Ferguson,† K.-Y. Chien,‡ W. Glowacki,‡ and P. Collins†
Naval Surface Warfare Center, Silver Spring, Maryland
and
H. Glaz§
University of Maryland, Silver Spring, Maryland
and
P. Colella¶
University of California, Berkeley, California

Abstract

This paper describes a numerical simulation of a planar shock reflecting from a dusty wedge. For the problem considered ($M = 10$, $\theta_w = 30$ deg), a double-Mach reflection (DMR) with an embedded wall jet is formed. The dust/air mixture on the wall was modeled as a dense gas, thereby focusing on how the dust mass influences the dynamics of the flow. The flow field was calculated by means of a high-order Godunov scheme that solves the nonsteady equations of gasdynamics. An adaptive mesh technique was used to follow the details of the Mach stem region. Flow visualization showed that the slipline from the main triple point became unstable and rolled up into positive rotational structures, which were entrained in the outer region of the wall jet. In addition, the velocity field induced by these structures caused the wall shear layer to become unstable and roll up into negative rotational structures that entrained dust from the fluidized bed. Vortex structures from the two shear layers paired, thus forming a chaotic flow that destroyed the coherence of the jet. Similarity coordinates were used to analyze this chaotic flow, thereby determining the mean-flow profiles and rms (root-mean-square) fluctuations in the jet and wall boundary layer. Thus, we time-average the *solution* — not the equations. This approach can be

* Senior Staff Scientist, currently with Lawrence Livermore National Laboratory
† Mathematician
‡ Aerospace Engineer
§ Professor, Mathematics
¶ Professor, Mechanical Engineering Department

used to calculate turbulent mixing in new types of flows where the turbulence models have not been verified.

I. Introduction

Mach reflection is a common feature of explosions occurring above surfaces. The shock structure changes from regular reflection to Mach reflection at a ground range approximately equal to the height of burst. A DMR shock structure is formed if the incident shock Mach number is greater than about 2.5. Detailed numerical calculations have been performed for the reflection of a high-explosives-driven blast wave from a planar surface.[1] A prominent fluid-dynamic feature of that DMR flow was a supersonic wall jet. Because of computer limitations at that time, we could only capture the laminar flow solution. Recent DMR experiments[2] have shown that the wall jet is turbulent. In addition, for many practical applications such as explosion safety, the Mach reflection occurs on a dusty surface (e.g., explosions in coal mines, where the dust is initially distributed along the mine walls), and a dusty boundary layer is formed. This paper investigates a simplified version of such problems, namely the DMR of a planar shock from a dusty wedge. Special attention is focused on the turbulent wall jet and dusty boundary layer region of the flow.

The Mach reflection of shock waves was discovered more than 100 years ago by the use of a spark shadowgraph technique in the pioneering experiments conducted in 1878 by Ernst Mach.[3] The triple-shock theory describing the states surrounding a Mach stem triple point was derived in 1943 by von Neumann[4]; also, analytic studies have been published.[5,6] The 1945 discovery of a complex Mach reflection may be attributed to Smith,[7] who first noticed a "kink" in the reflected shock. The DMR shock structure was discovered a few years later in 1951 by White,[8] who performed experiments with somewhat stronger shocks. A number of researchers[9,10] have tried to establish the boundaries of the various reflection regimes as a function of shock Mach number and wedge angle. Much of the recent experimental work is summarized in one review article.[11]

A number of numerical simulations of Mach reflections from wedges have been performed; some of the most successful efforts are the systematic studies[12,13] using a high-order Godunov scheme. However, these calculations have exclusively investigated the laminar flow regime. This paper specifically investigates the details of the unstable, fluctuating flow regions.

Recently we pursued a new approach—making a direct calculation of the turbulent mixing by following the dynamic evolution of the large-scale turbulent eddies on the computational grid. This approach was used to study turbulent fluctuations in free shear layers[21] and precursed airblast flows,[14] and to simulate the turbulent, dusty boundary layer behind a shock.[15]

The paper describes an extension of such direct calculations of the turbulent mixing. The problem considered is the reflection of a planar, constant-velocity shock from a wedge covered by a loose dust bed. The calculated turbulent environment was stored along similarity lines, and the solution was time-averaged to produce both the mean and rms profiles of the turbulent wall jet and dusty boundary layer flow. The formulation of the calculation is described in section II. The results are presented in section III, followed by a summary and conclusions in section IV.

II. Formulation

The problem considered here is the DMR flow field created by the reflection of a constant-velocity shock (Mach number, $M_I = 10$) from a 30-deg wedge that was covered with a loose dust bed (see Fig. 1).

The dynamics of the flow was governed by the two-dimensional (2-D), inviscid conservation laws of gas dynamics:

$$\frac{\partial}{\partial t}\rho + \nabla \cdot (\rho \mathbf{u}) = 0 \tag{1}$$

$$\frac{\partial}{\partial t}\rho \mathbf{u} + \nabla(\rho \mathbf{u}\mathbf{u}) = -\nabla p \tag{2}$$

$$\frac{\partial}{\partial t}\rho E + \nabla \cdot (\rho E \mathbf{u}) = -\nabla \cdot (p\mathbf{u}) \tag{3}$$

where $\mathbf{u}$ denotes the velocity and E represents the total energy ($E = e + 0.5\mathbf{u} \cdot \mathbf{u}$). The pressure p was related to the density ρ and internal energy e by the perfect gas equation of state:

$$p = (\gamma - 1)\rho e \tag{4}$$

where γ represents the constant ratio of specific heats and $\gamma = 1.4$. The equations were integrated numerically by means of a high-order Godunov scheme.[16]

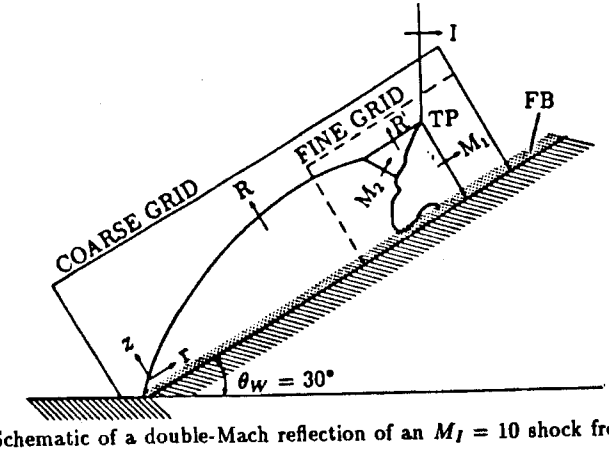

Fig. 1 Schematic of a double-Mach reflection of an $M_I = 10$ shock from a dusty wedge.

A two-dimensional Cartesian grid aligned with the wedge wall was used for the computational mesh. This consisted of a fine-mesh region ($100 \leq i \leq 600$ with initial $\Delta r = 0.025$ m; $1 \leq j \leq 322$ with initial $\Delta z = 0.025$ m) that followed the DMR structure; and a stretched-mesh region ($1 \leq i < 100$ with Δr variable) to capture the flow behind the DMR structure.

The mesh was initialized with ambient conditions in the air (state 1):

$$p_1 = 1.01325 \times 10^6 \text{dy/cm}^2; \rho_1 = 1.293 \times 10^{-3} \text{g/cm}^3;$$
$$e_1 = 1.96 \times 10^9 \text{erg/g}; u_1 = 0$$

and a three-cell-thick fluidized dust bed (subscript FB):

$$p_{FB}/p_1 = 1; \rho_{FB}/\rho_1 = 38.67;$$
$$e_{FB}/e_1 = 0.0258; u_{FB} = 0$$

along the wedge wall ($10\text{m} \leq r \leq \infty$; $0 \leq j \leq 3$).

The left boundary of the mesh $(0, z, t)$ was driven by the conditions (state 2) behind an $M_I = 10$ shock:

$$p_2/p_1 = 116.5; \rho_2/\rho_1 = 5.71; e_2/e_1 = 20.39;$$
$$u_2/a_1 = 7.145; v_2/a_1 = -4.125 (\theta_w = 30).$$

Wall drag was neglected at the bottom of the fluidized bed, hence an inviscid, slip boundary condition ($v = 0$, $\partial u/\partial z = 0$, $\partial p/\partial z = 0$) was used at the bottom boundary. A sliding inflow boundary condition (corresponding to the state behind the incident shock) was used at the top boundary of the mesh to drive the reflection process.

As will be shown (e.g., see Fig. 6), major features of the flow, such as the foot of the Mach stem, $R_S(t)$ and the moving stagnation point $R_{SP}(t)$, move at constant velocity. This allows one to define a similarity variable[17]

$$\xi = [r - R_{SP}(t)] / [R_S(t) - R_{SP}(t)]$$

that represents constant similarity positions along the wall jet. Anticipating the turbulent nature of the flow, the flow field was sampled during each computational cycle at the following similarity locations:

$$\xi = 0, 0.2, 0.4, 0.6, 0.8, 1.0 \qquad \text{(wall jet region)}$$

$$\xi = -0.5, -1.0, -2.0 \qquad \text{(boundary layer region)}$$

and stored for later statistical analysis of the turbulence.

The dust-air mixture in the fluidized bed was treated as a continuum fluid with an initial density of 50 mg/cm^3. An equilibrium, dense-gas (DG) model was used as the equation of state of the mixture, namely,

$$p = (\gamma - 1)\rho e \text{ with } \gamma = 1.4 \qquad (4)$$

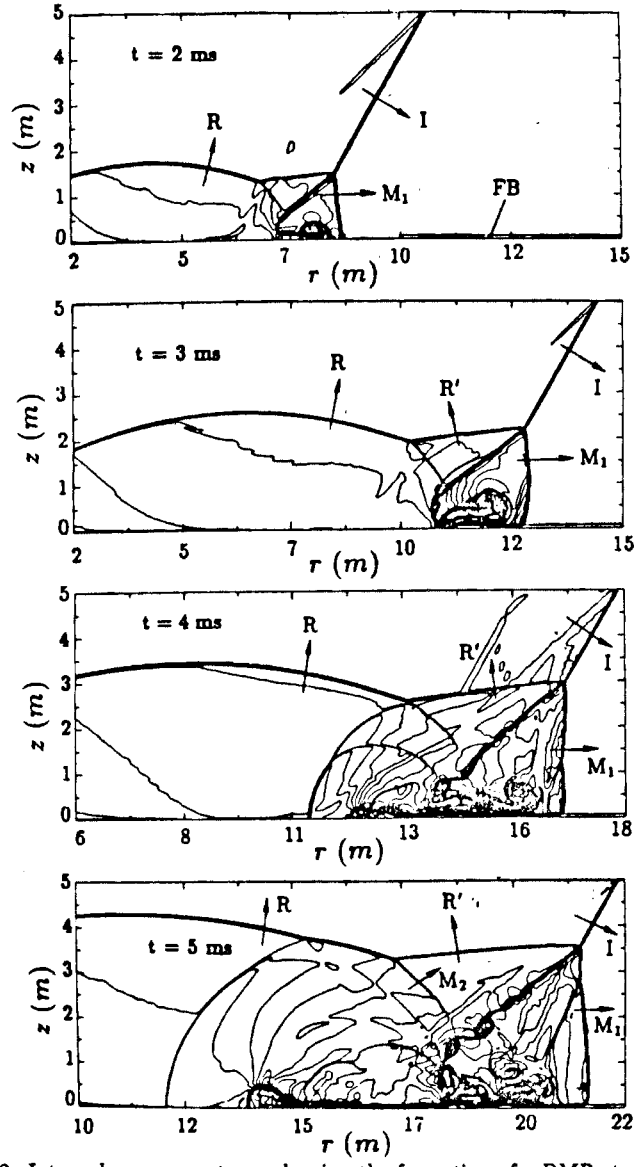

Fig. 2 Internal energy contours showing the formation of a DMR structure on the wedge ($t = 2$ ms), interaction with the leading edge of the fluidized bed ($t = 3$ ms),

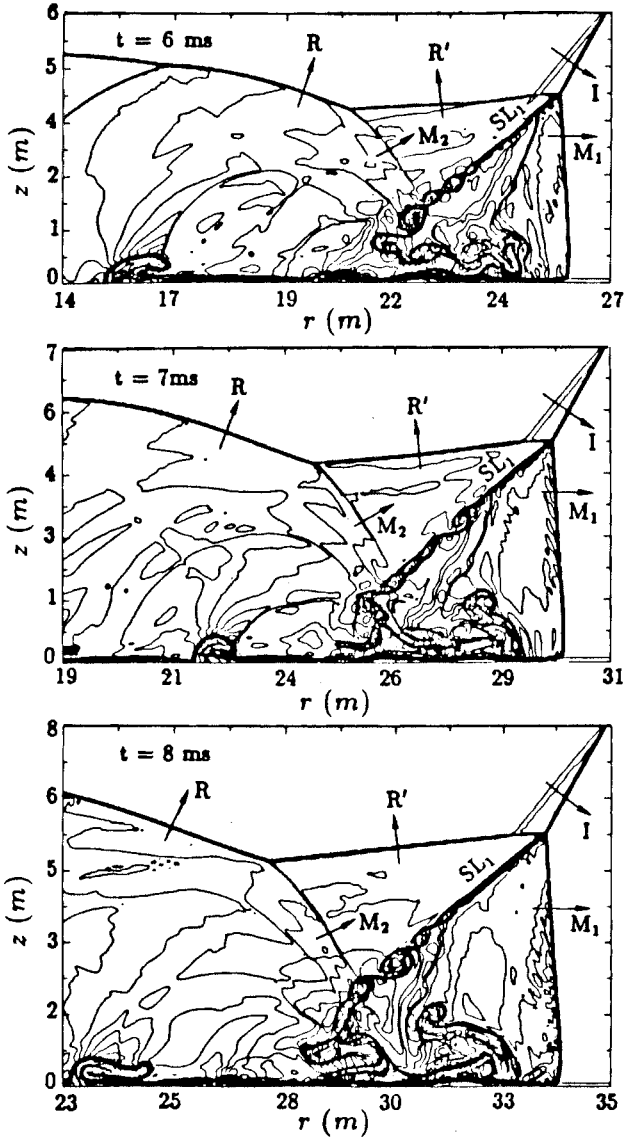

Fig. 3a Evolution of the turbulent wall jet from $t = 6 - 11$ ms.

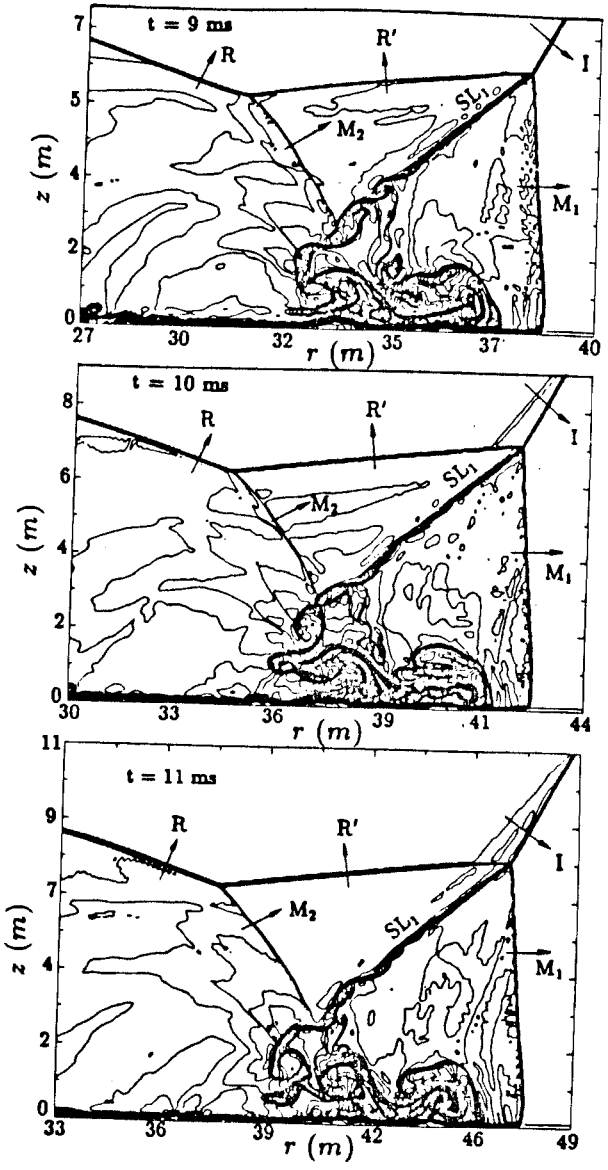

Fig. 3b Evolution of the turbulent wall jet from $t = 6 - 11$ ms.

In the past, this DG model has been shown to accurately simulate turbulent boundary layer flows for the case of very small diameter dust particles.[15]

The calculation was run for 5000 computational cycles to accumulate enough data for a good statistical analysis of the turbulent flow. This required about 10 hours on the Cray XMP computer. The results are described in the next section.

III. Results

A. Flow Visualization

Figure 2 presents internal energy contours at various times near the beginning of the calculation (t = 2 to 5 ms). They show the initial formation of the DMR shock structure and laminar wall jet and its interaction with the leading edge of the fluidized bed, FB. The flow is unstable and rapidly becomes chaotic.

Figure 3 presents a series of snapshots of the flow that show the evolution of the DMR flow from t = 6 to 11 ms. Turbulent mixing impedes the coherent progress of the jet; the tip of the jet slows and then folds back on itself (t = 8 to 9 ms). The wall jet is re-energized at t = 11 ms ($r \simeq$ 39 m) and flows forward. This pulsating action of the jet sends acoustic waves forward that perturb the foot of the Mach stem.

Figure 4 gives a more detailed view of the flow field at t = 32 ms. The internal energy contours (Fig. 4a) clearly show the growth of rotational structures on the slip line (SL_1) from the main triple point (TP_1). These rotational structures are swept forward near the wall and form the free shear layer (FSL) of the wall jet flow. The pressure contours (Fig. 4b) show that the mixing on the slip line and in the wall jet is an isobaric process similar to that occurring in low-speed turbulent flows. In addition, Fig. 4b shows weak acoustic waves emanating from the moving stagnation point region (SP); these were generated by turbulent fluctuations in the boundary layer along the wall, and are carried aft by the pressure characteristics. Figure 4c presents the vorticity contours of the same flow field. The solid lines denote positive vorticity contours on the slip line SL_1, and free shear layer FSL; the dashed curves denote negative vorticity contours from the boundary layer region. The velocity field from the vortex structures on the free shear layer trips the wall boundary layer and causes it to roll up locally. There is a pairing of the boundary layer vortex structures with the free shear layer vortex structures that causes the boundary layer to separate locally from the wall at many locations along the jet. This phenomenon is similar to the strong interactions found in low-speed wall jets.[18] The entropy contours (Fig. 4d) also show this effect; material from above the free shear layer mixes all the way to the wall, and dust from the fluidized bed mixes to the top of the free shear layer. Note that conventional turbulence models are not designed to simulate such strong interactions between two shear layers containing vorticity of opposite signs.

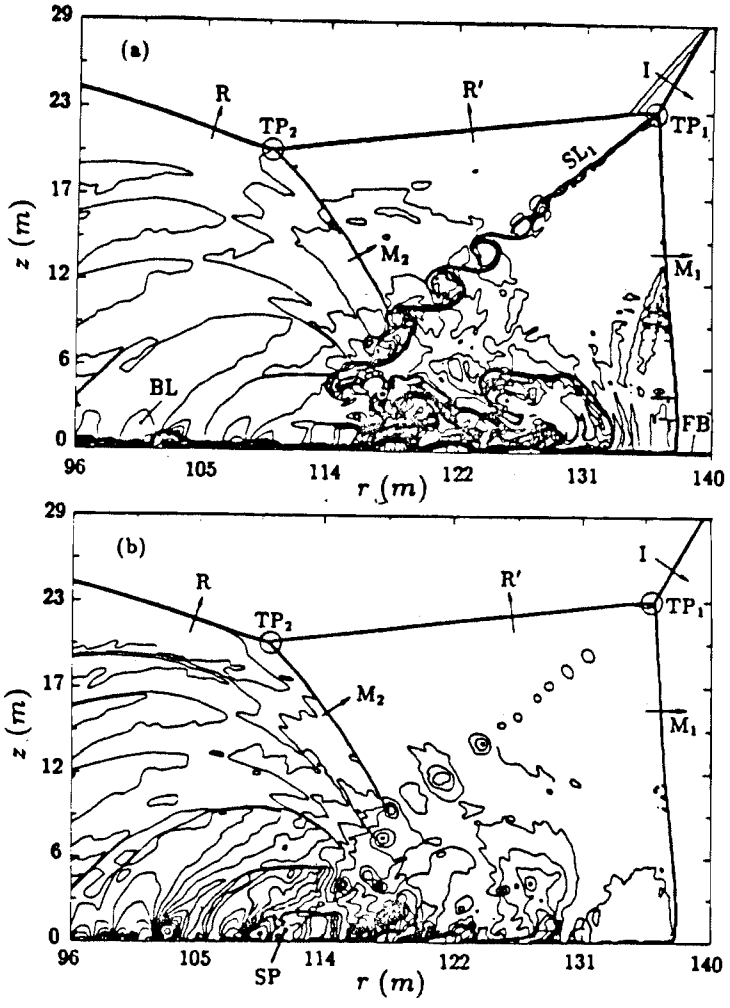

Fig. 4a Detailed flow field contours at t = 32 ms: (a) energy, (b) pressure.

B. Similarity Scaling of the DMR Flow

Figure 5 depicts the environment at the top of the fluidized bed a a time of 32 ms. Clearly, the flow is quite chaotic, and it is fruitles to compare point values of the environment time histories. Instead, w chose the traditional approach of reporting the time-averaged profiles of th turbulent flow.

Since the problem considered here is the reflection of a square-wave shoc and not a decaying blast wave, the gas-dynamic flow field contains no cha

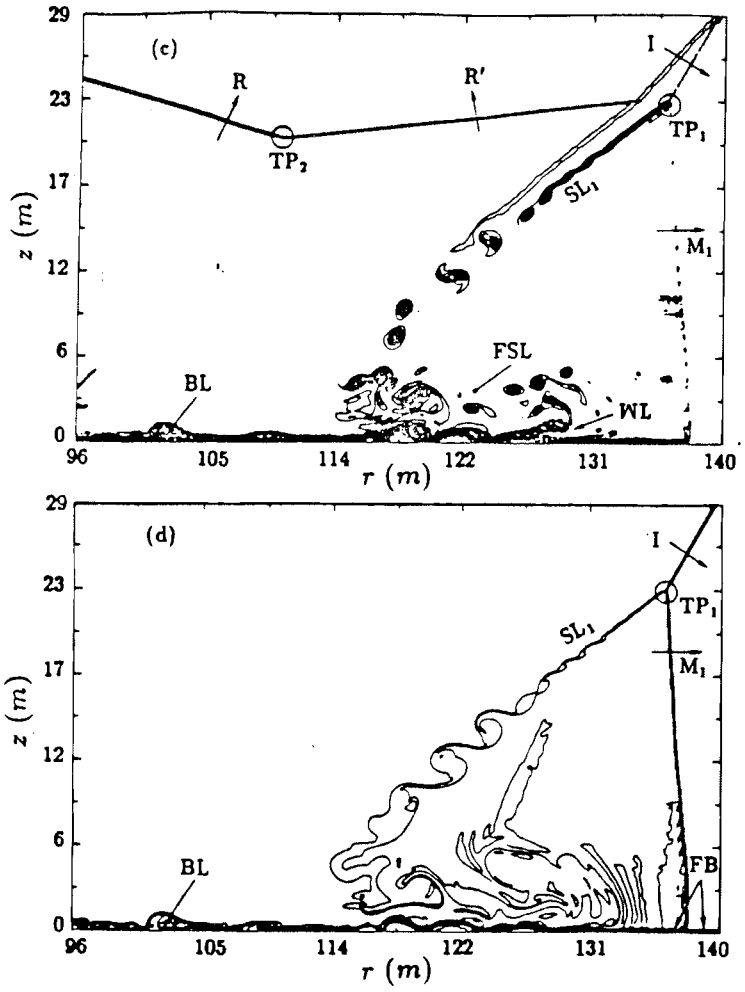

Fig. 4b Detailed flow field contours at t = 32 ms: (c) vorticity (d) entropy.

acteristic length scale other than the distance the shock has traveled up the wedge. Under such circumstances, dimensional analysis[17] suggests that the problem is self-similar and the independent variables can be reduced from three (r, z, t) to two: $x \sim r/t$ and $y \sim z/t$. In these coordinates, the laminar solution would remain constant, independent of time. We demonstrate below that the calculated solution satisfies the similarity constraints, and we define the similarity coordinates that were used to time-average the turbulent flow.

Figure 6 presents a time-distance diagram for the calculation. It shows that both the foot of the Mach stem $R_S(t)$ and the moving stagnation point

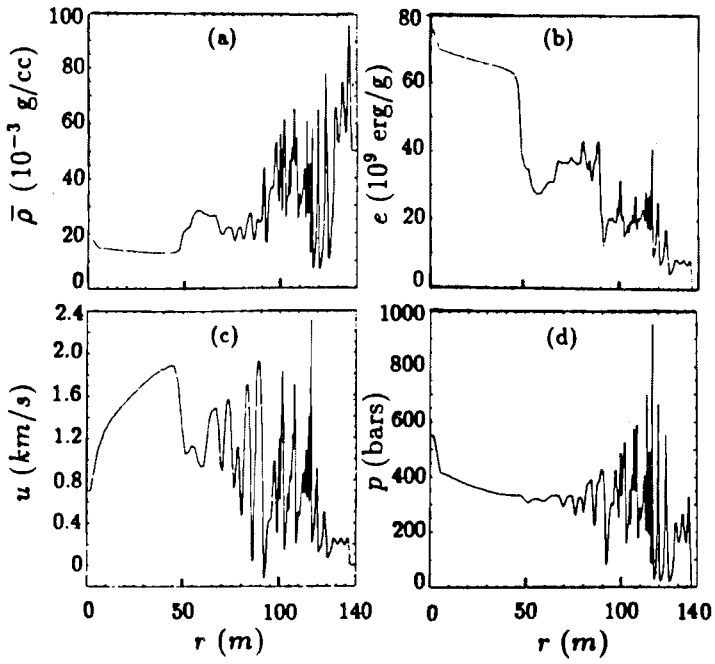

Fig. 5 Flow field along the top of the fluidized bed at t = 32 ms: (a) density, (b) internal energy, (c) velocity, (d) pressure.

$R_{SP}(t)$ move with constant velocity, according to

$$R_S(t) = 4.29t \tag{5}$$

$$R_{SP}(t) = 3.5t \tag{6}$$

where $[R]$ = m and $[t]$ = ms. Hence, the length L of the DMR region grow linearly with time:

$$L(t) \equiv R_S(t) - R_{SP}(t) = 0.79t. \tag{7}$$

This suggests a similarity scaling in the r direction of the following:

$$\xi = [r - R_{SP}(t)] / L(t) \tag{8}$$

as mentioned previously. Figure 6 also depicts the height of the triple poin $Z_{TP}(t)$, vs time; it shows that the triple point grows with a constant vertic velocity according to:

$$Z_{TP}(t) = 0.72t \tag{9}$$

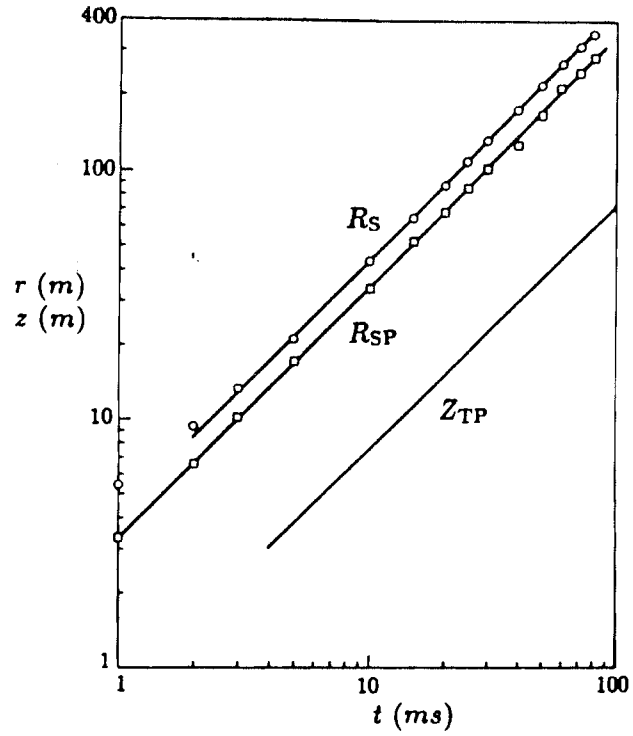

Fig. 6 Location of the Mach stem shock (R_S)moving stagnation point (R_{SP}), and triple point (Z_{TP}) vs time.

where $[Z]$ = m and $[t]$ = ms. This indicates that the vertical scale of the DMR flow field grows linearly with time and suggests a similarity scaling of $z/Z_{TP}(t)$, or equivalently:

$$y = z/L(t) \tag{10}$$

since $Z_{TP}(t)/L(t) = 0.72t/0.79t = 0.911$.

To identify characteristic values of y, such as the boundary layer thickness, one must consider the flow field profiles near the wall. To that end the flow field was time-averaged along lines of ξ = constant, using the last 3625 cycles of the calculation (t = 16 to 592 ms). Examples of the mean-flow profiles in the wall jet region are shown in Fig. 7. The mean velocity profiles (Fig. 7a) do indeed resemble those expected for a wall jet; the stream-wise velocities reach a peak value of about 5.3 km/s in the jet and decay to a value of about 3.5 km/s far above the wall. Mean density profiles are shown in Fig. 7b. The fluidized bed was compressed somewhat ($\bar{\rho} \sim 65$ mg/cm^3) by the Mach stem shock. The profiles converge at a height of $z \simeq 2.15$. As in previous experimental studies,[19] this convergence point z_o was used to define the calculated mean height of the fluidized bed. Inside the fluidized

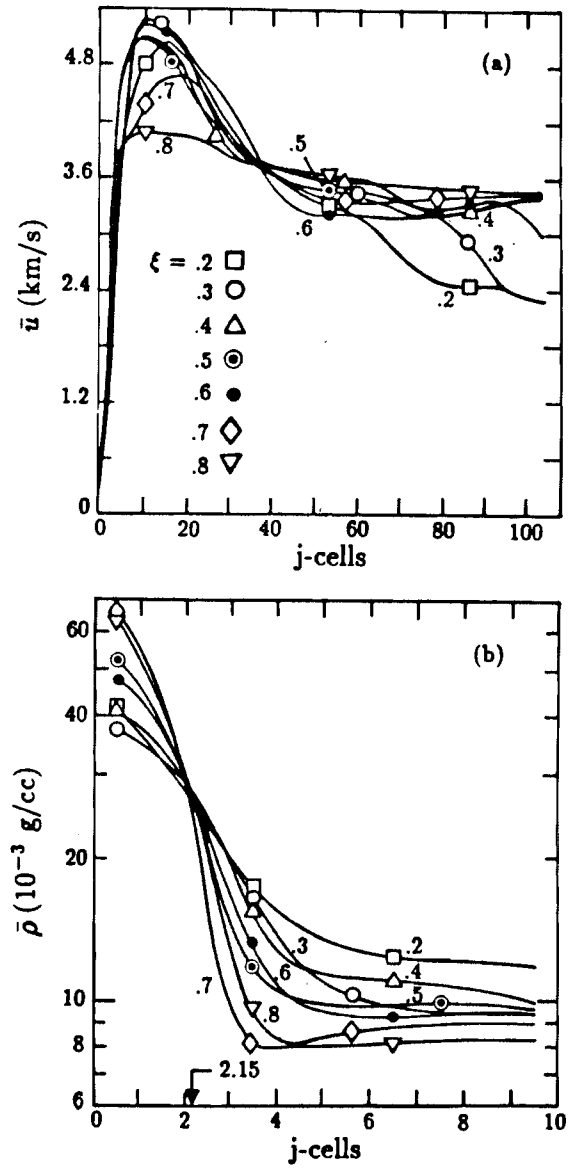

Fig. 7 Calculated mean profiles in the wall jet region: (a) stream-wise velocity, (b) density.

bed ($z < z_o$), the densities remain large (e.g., values of 40 to 60 mg/cm^3), demonstrating that turbulent scouring has not severely depleted the mass in the layer. In the boundary layer above the fluidized bed ($z > z_o$), turbulent mixing causes the density profiles to become thicker as the distance behind the shock increases.

These profiles are idealized in Fig. 8. In the wall jet region (Fig. 8a) one can define the following characteristic parameters:

1. U_m, the local maximum stream-wise velocity, and its corresponding height y_m.
2. U_e, the local edge velocity above the jet, and its height $y_e > 3y_m$.
3. $U_* = (U_m + U_e)/2$, the local average velocity at the center of the free shear layer region of the jet, and its corresponding height y_*.
4. The local boundary layer height y_{BL}, where $\bar{u} = 0.99U_m$.
5. And the height of the fluidized bed, y_o.

In the region behind the DMR structure (Fig. 8), one can similarly define local boundary layer parameters:

1. U_∞, the local freestream velocity above the boundary layer.
2. y_{BL}, the boundary layer height, where $\bar{u} = 0.99U_\infty$.
3. And the height of the fluidized bed, y_o.

Figure 9 depicts the variation of these calculated profile parameters as a function of ξ, the nondimensional distance along the wall. Figure 9a shows the variation of the characteristic heights y_*, y_m, and y_{BL} that will be used to scale the profiles in the y direction. Figure 9b presents the characteristic velocities that will be used to nondimensionalize the local velocity profiles. The velocities reach a maximum value of more than 5 km/s in the jet, and decay to about 2 km/s far behind the DMR region. Figure 9c depicts the mean pressure and density above the wall jet (subscript e) and above the boundary layer (subscript ∞) as a function of ξ. They reach a peak value near the moving stagnation point ($\xi = 0$); then the strong expansion wave (represented by the dashed portion of the curve) accelerates the flow forward and supports the wall jet.

C. Wall Jet Profiles

Figure 10 presents the time-averaged mean-flow profiles of the wall jet. The profiles are nondimensionalized by the appropriate local peak values from Figure 9, and scaled by the wall jet similarity variable

$$\eta_J = (y - y_o)/(y_* - y_o) \tag{11}$$

which equals 1 at the centerline of the free shear layer and 0 at the top of the fluidized bed. The similarity scaling has removed the time dependence of the flow. The wall-jet variable η_J seems to collapse the $\bar{u}/U_m$ velocity profiles, especially in the free shear layer region ($0.5 < \eta_J < 1.5$). How-

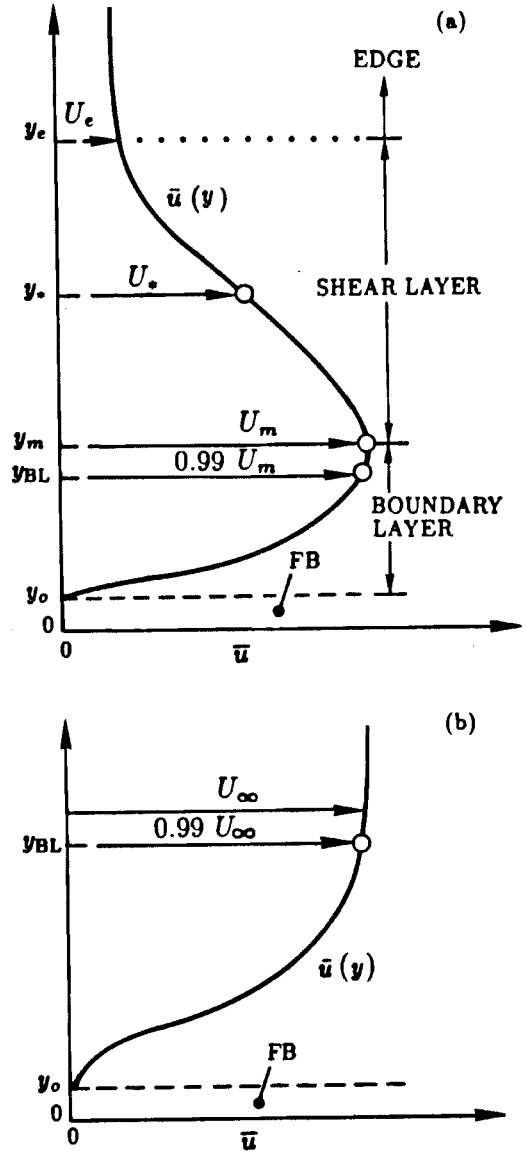

Fig. 8 Schematic of the mean-flow velocity profiles: (a) wall jet region, (b) trailing boundary layer ($\xi < 0$).

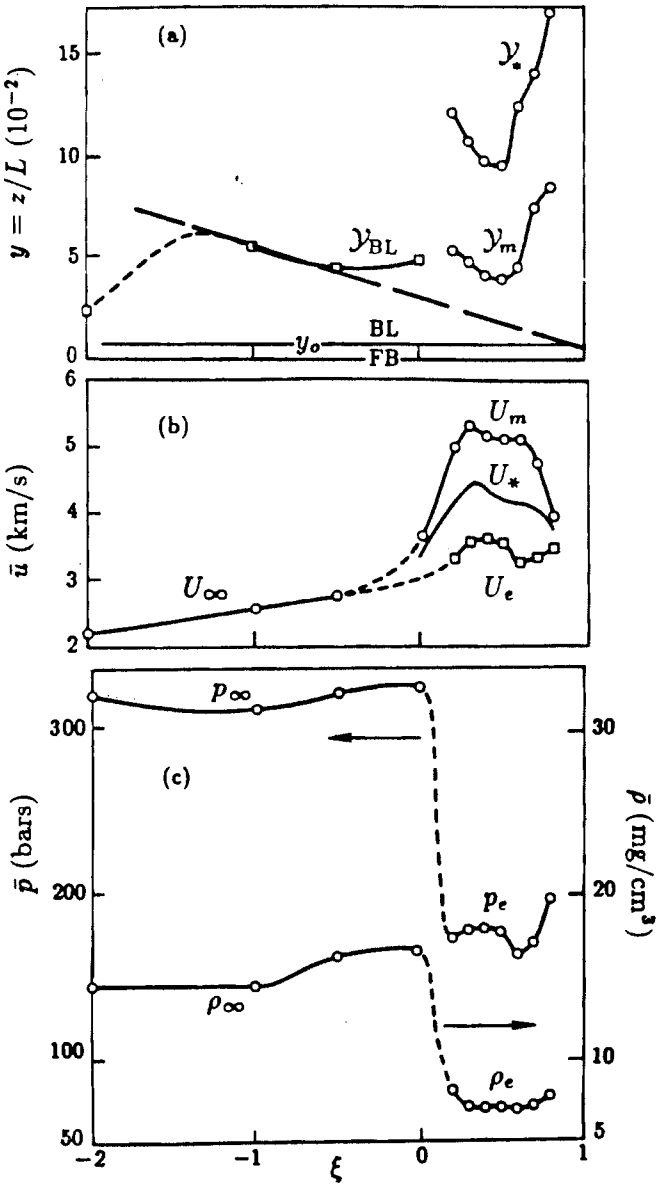

Fig. 9 Profile parameters as a function of distance ξ: (a) shear layer (y_*) and boundary layer (y_{BL}) heights, (b) local peak velocities, (c) local mean pressures and densities.

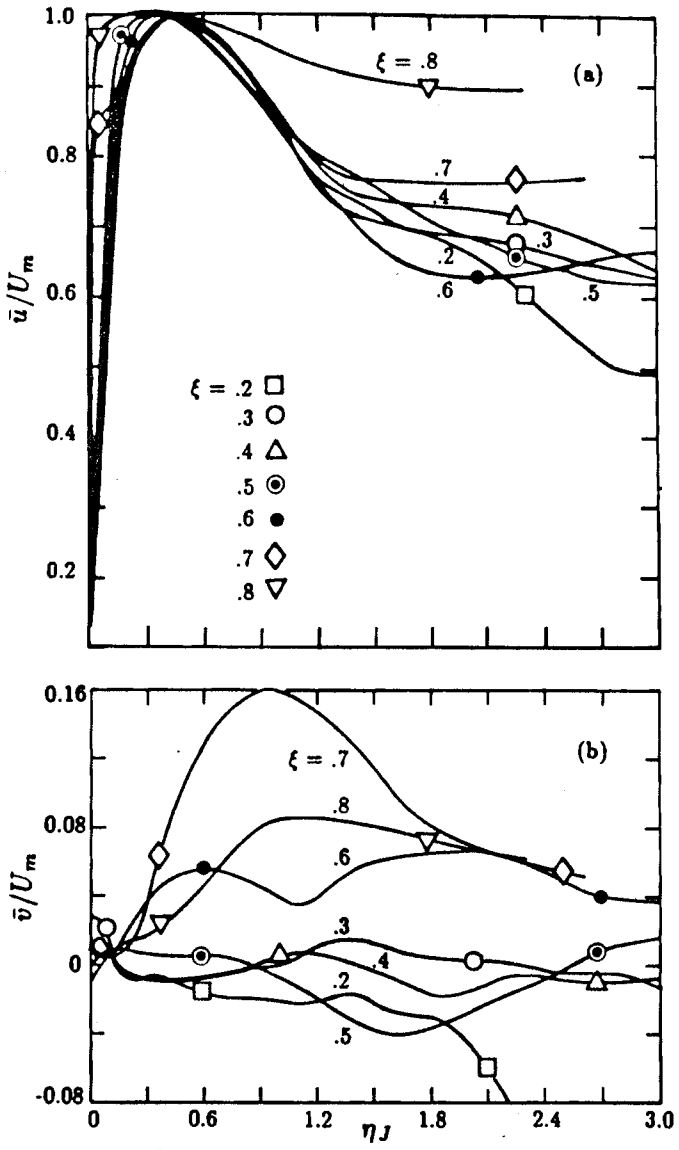

Fig. 10a Mean-flow profiles of the wall jet: (a) stream-wise velocity, (b) transverse velocity.

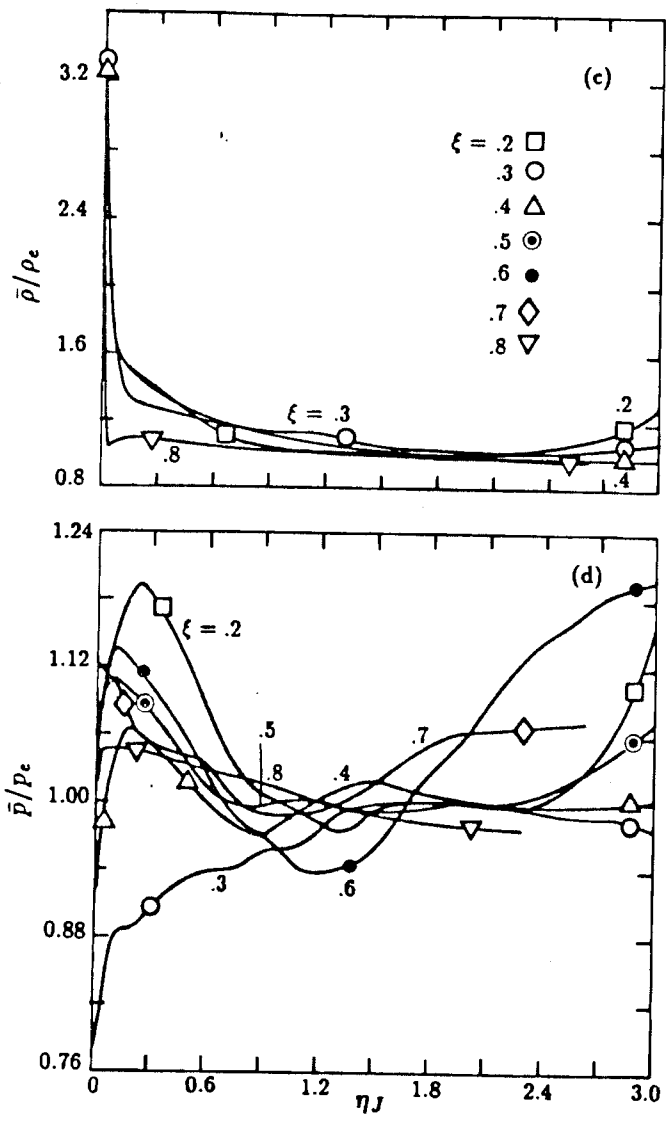

Fig. 10b Mean-flow profiles of the wall jet: (c) density, (d) pressure.

ever, the profiles are still functions of ξ; for example, at the front of the jet ($\xi \simeq 0.8$), the boundary layer and free shear layer are decoupled by a constant-velocity plateau. Near the front vortex ($\xi \simeq 0.7$) one can observe a separating boundary layer profile with an inflection point. Near the wall, the mean vertical velocities are positive because the turbulent fluctuations scour and entrain dust from the fluidized bed; the mean density values are large compared to the edge value ($\bar{\rho} \simeq 3\rho_e$) for the same reason. The mean pressures are relatively constant (except near $\xi = 0$), indicating an isobaric mixing process similar to other turbulent flows.

Figure 11 presents the rms fluctuating-flow profiles of the wall jet. The stream-wise velocity fluctuations (Fig. 11a) peak at about 0.30 near the wall ($\eta_J \simeq 0.1$) and near the centerline of the free shear layer ($\eta_J = 1$), but there were not enough computational cycles to achieve complete convergence of these second moments. The transverse velocity fluctuations (Fig. 11b) peak near $\eta_J = 0.6$ and are nonzero at the bottom of the boundary layer ($\eta_J = 0$) because of turbulent fluctuations from the fluidized bed. The Reynolds stress (Fig. 11c) peaks near the wall. The density fluctuations (Fig. 11d) are largest near the wall because of turbulent scouring of dust from the fluidized bed. Pressure fluctuations (Fig. 11e) range from 10 to 30% because the wall jet flow is supersonic.

D. Wall-Region Profiles of the Jet

Figures 12 and 13 focus on the wall region of the jet. The profiles were nondimensionalized by the appropriate local peak values (denoted by subscript m) from Fig. 9, and rescaled by means of the boundary layer variable

$$\eta_{BL} = [y - y_o]/[y_{BL} - y_o]. \qquad (12$$

Figure 12a depicts the calculated boundary layer profiles at various locations along the wall jet. Also shown in that figure are experimental profiles (denoted by the shaded regions) based on laser-Doppler velocimetry (LDV) measurements of velocity profiles of a turbulent boundary layer behind a planar shock propagating along both clean and dusty walls.[19] Between the Mach stem and the tip of the jet ($0.8 \leq \xi < 1$), there is very little dust involvement with the flow; hence, the calculated profiles agree with the clean boundary layer data and the $n = 1/7$ power function. This is a deficiency of the numerical simulation resulting from inadequate grid resolution in this region. Obviously there will be dust entrainment immediately behind the Mach stem shock. As the distance behind the Mach stem increases there is increasing dust involvement with the flow; hence, the calculated profiles systematically approach the dusty boundary layer data and the profile labeled DG3, which was calculated for a dusty boundary layer behind a planar shock.[15] Evidently there is no single boundary layer profile in the DMI region; instead, the profiles depend on ξ.

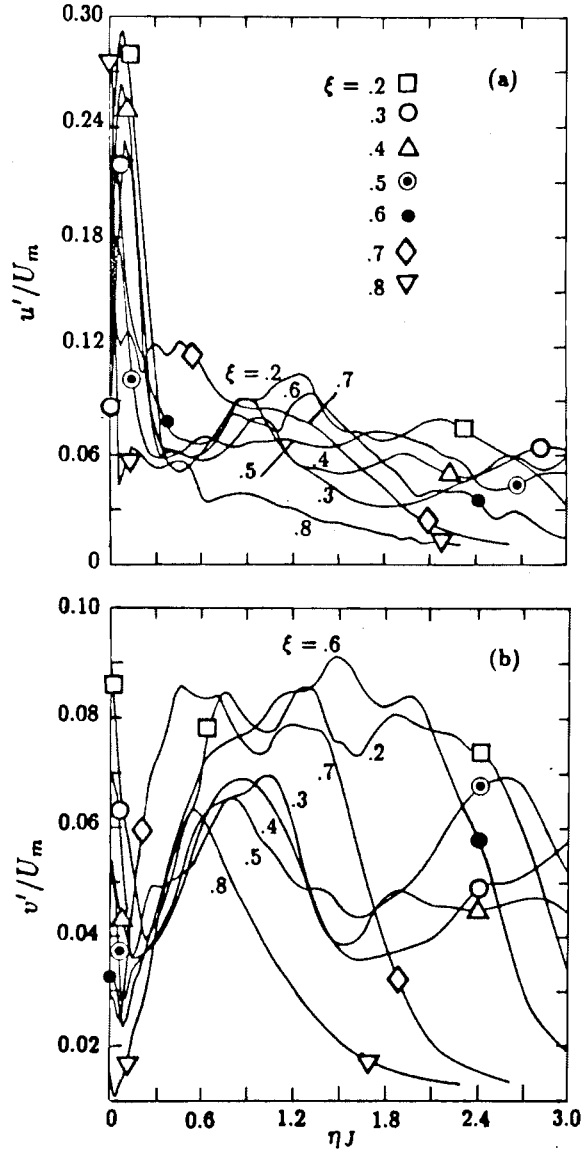

Fig. 11a RMS fluctuating-flow profiles of the wall jet: (a) stream-wise velocity, (b) transverse velocity.

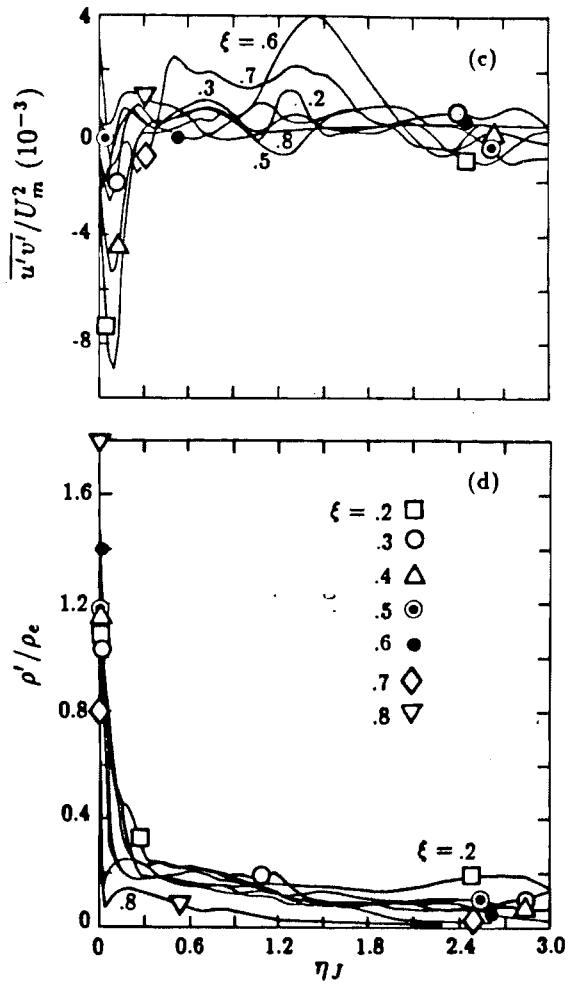

Fig. 11b RMS fluctuating-flow profiles of the wall jet: (c) shear stress, (d) density.

Figure 12b depicts the calculated specific volume profiles $\bar{\lambda}/\Lambda_m$ at various locations along the jet. Also shown in that figure are experimental profiles (denoted by the shaded region) based on streak x-ray measurements of dust density profiles for a turbulent boundary layer behind a planar shock propagating along a dusty wall.[19] The calculated specific volume ratios are near 1 except in the inner 20% of the boundary layer. They are well above the measured profiles for the planar shock case. Hence, the significant effects of the dust mass are confined to the near-wall region.

Figure 13 presents the rms fluctuating-flow profiles in the wall region of the jet. The u' fluctuations reach a peak value of about 0.28 U_m at

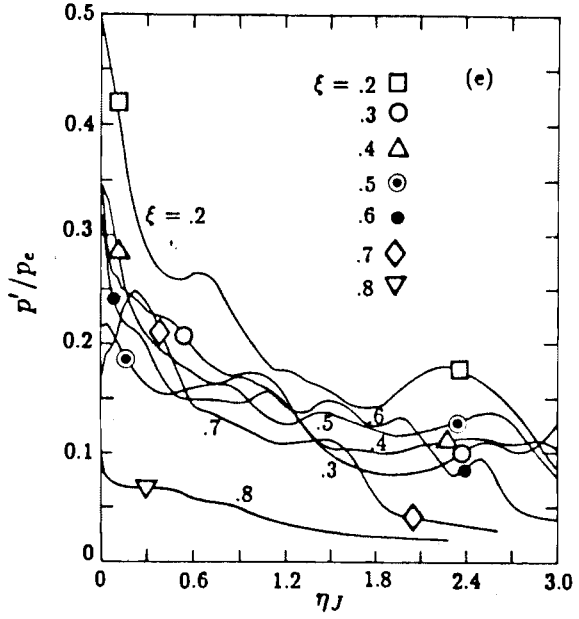

Fig. 11c **RMS fluctuating-flow profiles of the wall jet:** (e) pressure.

$\eta_{BL} = 0.25$, whereas the v' fluctuations reach a peak value of about 0.09 U_m at the bottom of the boundary layer. The Reynolds stress reaches a peak value of about -0.009 U_m^2 at $\eta_{BL} = 0.25$. The pressure fluctuations are essentially independent of height, and vary from 20 to 30% of p_m.

E. Boundary Layer Profiles Behind the DMR Structure

The calculated boundary layer profiles behind the DMR structure ($-2 \leq \xi \leq 0$) are presented in Figs. 14 and 15. The profiles were nondimensionalized by the local peak values (denoted by subscript ∞) from Fig. 9, and scaled by the boundary layer similarity variable, η_{BL}.

Figure 14 depicts the time-averaged mean-flow profiles. The boundary layer scaling seems to collapse these profiles quite well (except at $\xi = -2$, which is behind the leading edge of the fluidized bed rollup). The outer region of the boundary layer contains very little dust mass because of turbulent mixing; hence the $\overline{u}$ velocity profiles are near the clean flow $n = 1/7$ power function profile. Note in Fig. 14a that the stream-wise velocity is nonzero ($\overline{u}/U_\infty \simeq 0.5$) at the top of the fluidized bed, whereas its value was near 0 in the wall jet region. Perhaps the large-scale mean pressure gradient (see Fig. 9c) near $\xi = 0$ was able to accelerate the material in the fluidized bed to such values. Wall drag should be added to suppress this effect. Perhaps also the turbulent mixing has scoured most of the dust mass from the fluidized

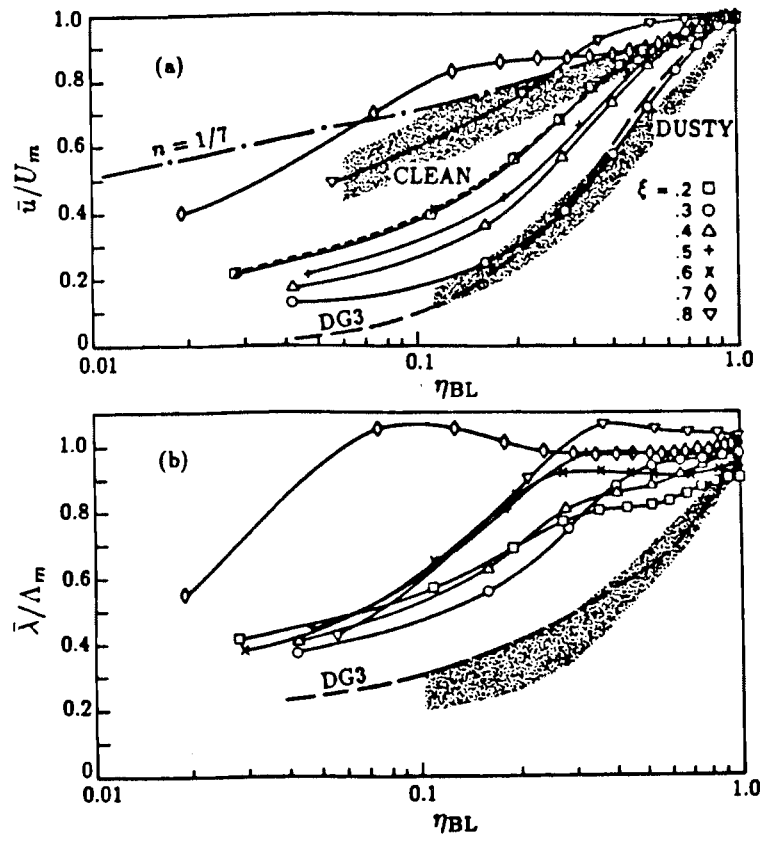

Fig. 12 **Mean-flow boundary layer profiles of the wall jet:** (a) stream-wise velocity, (b) specific volume ratio.

bed. Mass injection might be needed to maintain large dust densities in the fluidized bed at large distances behind the shock. Figure 14c shows that densities reached only about 1.5 ρ_∞ at $\eta_{BL} = 0$. The mean pressures were constant throughout the boundary layer.

Figure 15 depicts the rms fluctuating-flow profiles of the boundary layer behind the DMR structure. The u' reaches peak values of 20 to 25% of U_∞ at $\eta_{BL} = 0$. The Reynolds stress $\overline{u'v'}$ reaches a peak of about -0.004 U_∞^2; the profile for $\xi = -2$ indicates that station was laminar. Density fluctuations reached values as large as 30 to 50% of the freestream value (Fig. 15d). Pressure fluctuations ranged from 10 to 30% of the freestream value (Fig. 15e).

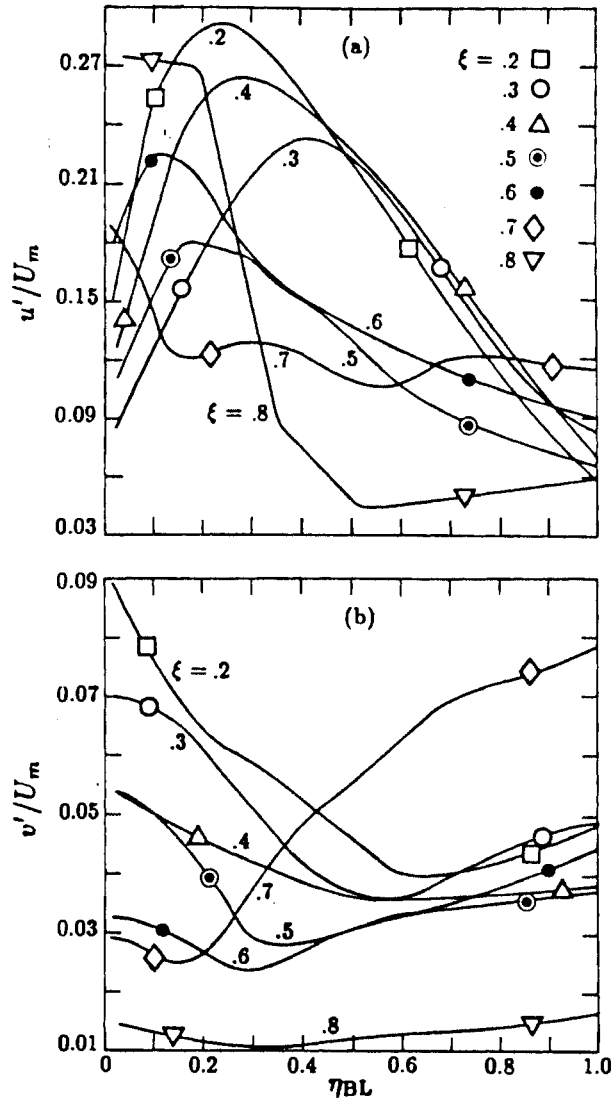

Fig. 13a RMS fluctuation profiles of the boundary layer of the wall jet ($0.2 \leq \xi \leq 0.8$): (a) stream-wise velocity, (b) transverse velocity.

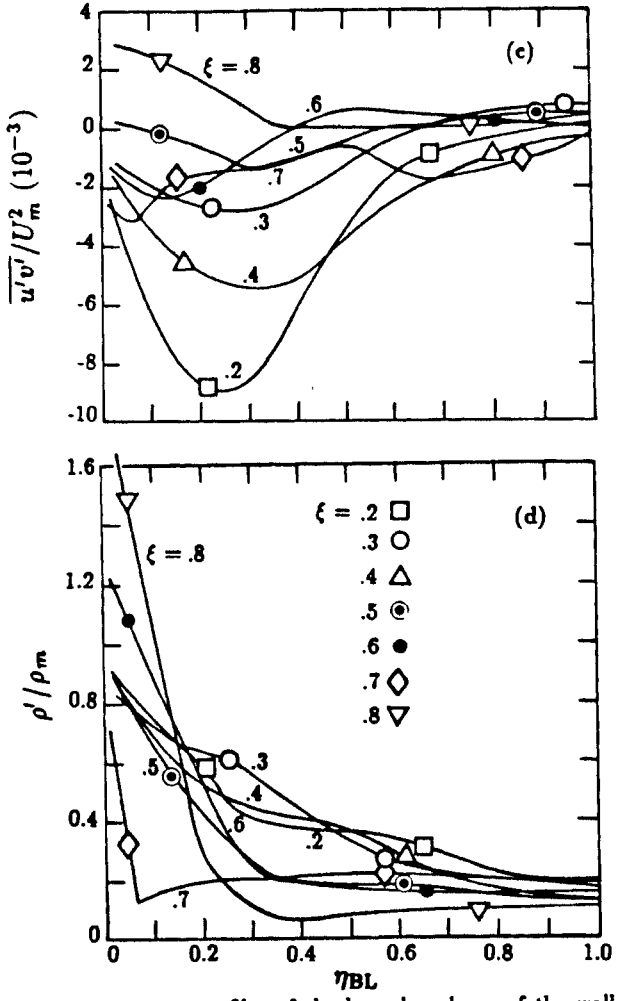

Fig. 13b RMS fluctuation profiles of the boundary layer of the wall jet ($0.2 \leq \xi \leq 0.8$): (c) Reynolds stress, (d) density.

F. Boundary Layer Growth

Let us define the boundary layer thickness, δ, as the boundary lay height above the fluidized bed:

$$\delta = z_{BL} - z_o. \tag{1}$$

Nondimensionalizing this by the distance R_s that shock has propagated alo the wedge gives:

$$\delta/R_s = (y_{BL} - y_o)b/R_s$$
$$= 0.184(y_{BL} - y_o). \tag{1}$$

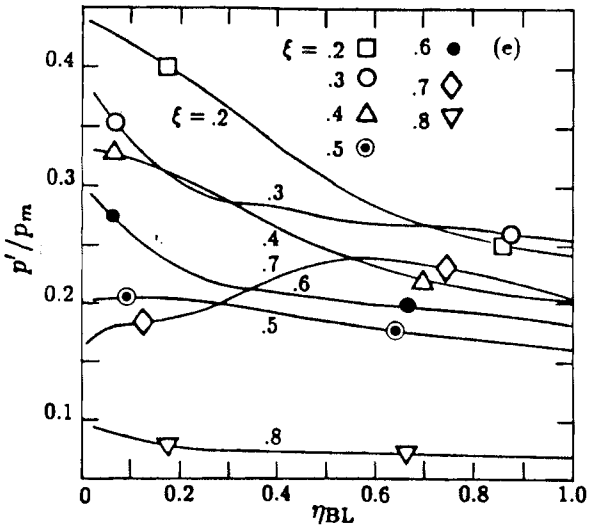

Fig. 13c RMS fluctuation profiles of the boundary layer of the wall jet ($0.2 \leq \xi \leq 0.8$): (e) pressure.

For boundary layer analysis, it is more convenient to consider the nondimensional distance along the wedge:

$$x = r/R_s \tag{15}$$

rather than the wall jet length ξ. Of course, they are linearly related by

$$\begin{aligned} x &= R_{SP}/R_s + \xi L/R_s \\ &= 0.816 + 0.184\xi. \end{aligned} \tag{16}$$

Figure 16 presents the calculated dusty boundary layer thickness δ/R_s as a function of x. The boundary layer starts at the foot of the Mach stem ($x = 1$) and rapidly balloons upward due to the separating flow at the tip of the wall jet ($x \simeq 0.94$). The boundary layer continues to grow with increasing distance behind the Mach stem. It reaches a peak value of about $\delta/R_s \simeq 0.009$ at $x = 0.63$, and then decays to zero at the leading edge of the dusty layer ($x = 0.35$).

Note that the boundary layer thickness continues to grow in the stagnation point region ($x = 0.82$). Previous analytic solutions[20] *assumed* that the boundary layer thickness was zero at the moving stagnation point. Figure 16 shows that this is clearly incorrect.

IV. Summary and Conclusions

The slip line emanating from the Mach stem triple point is unstable. The experiments of Matsuo et al.[2] show that coherent rotational structures

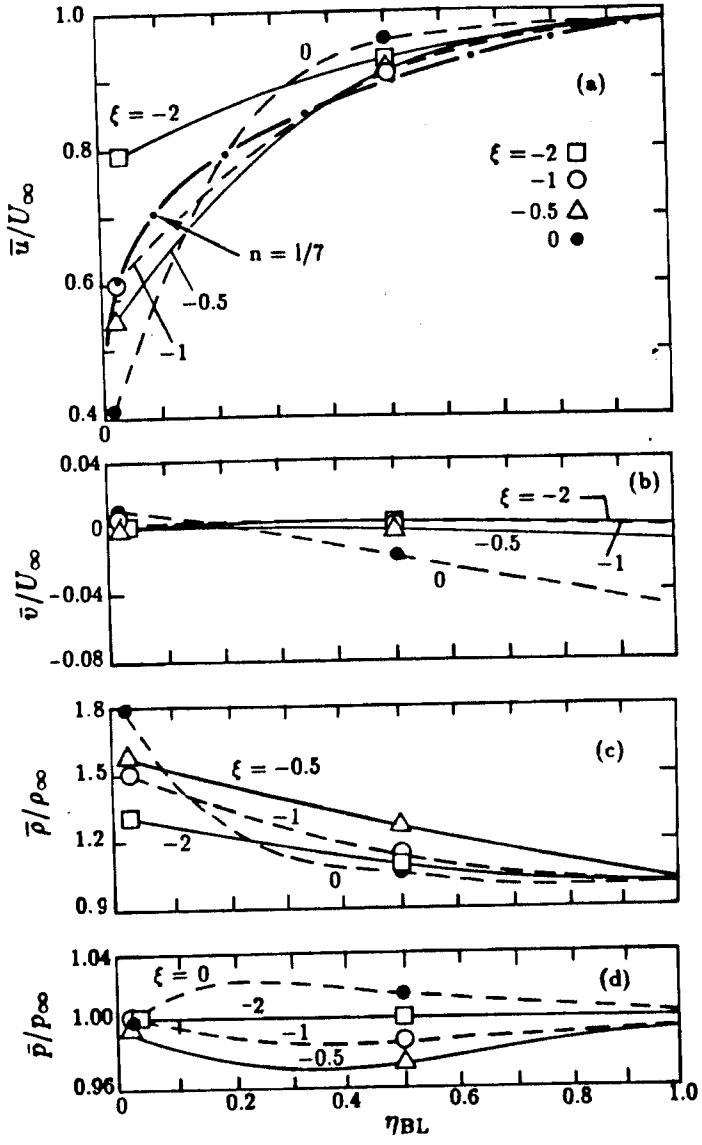

Fig. 14 Mean-flow boundary layer profiles behind the DMR structure ($-2 \leq \xi \leq 0$): (a) stream-wise velocity, (b) transverse velocity, (c) density, (d) pressure.

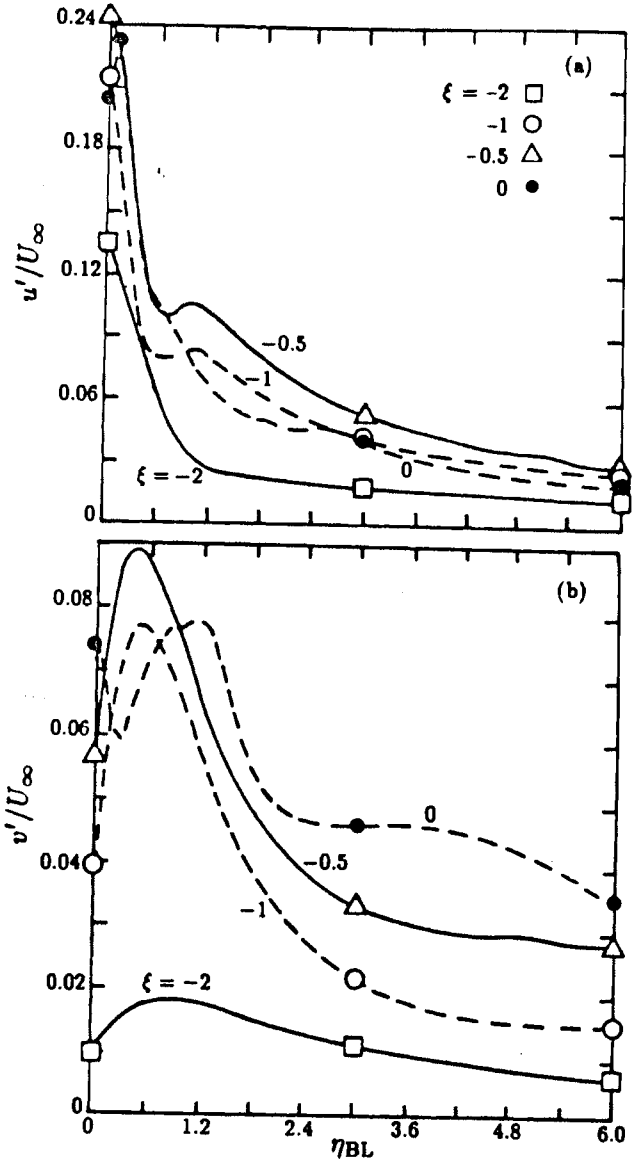

Fig. 15a RMS fluctuating-flow profiles of the boundary layer behind the DMR structure ($-2 \leq \xi \leq 0$): (a) stream-wise velocity, (b) transverse velocity.

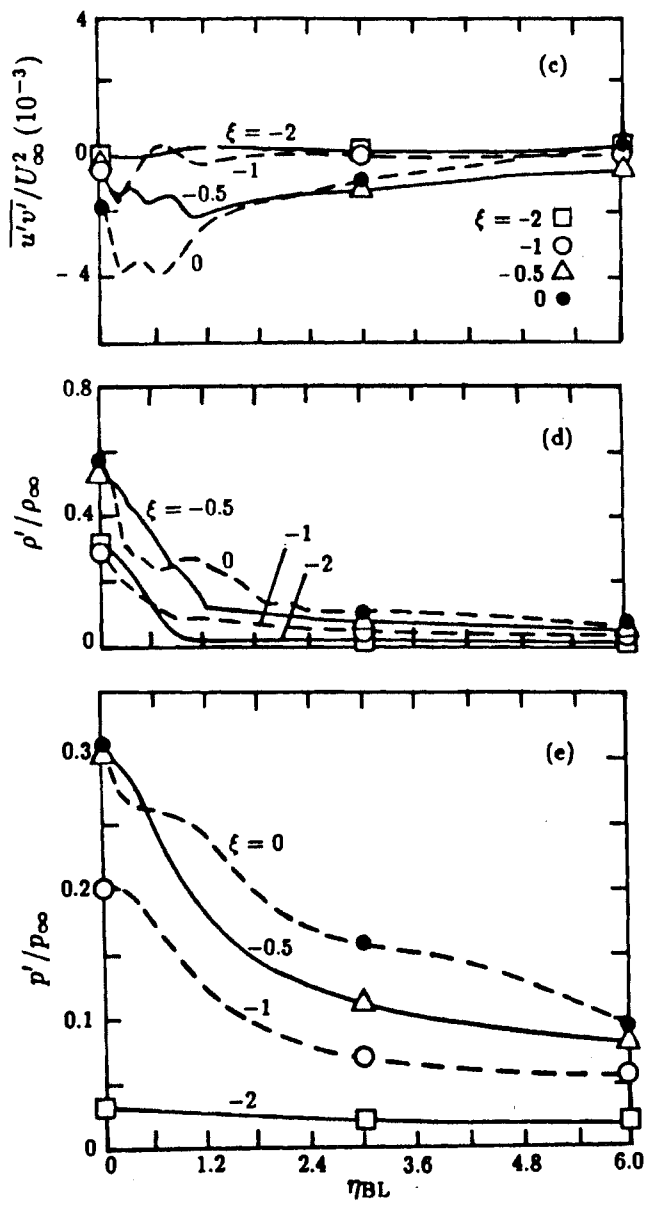

Fig. 15b RMS fluctuating-flow profiles of the boundary layer behind the DMR structure ($-2 \leq \xi \leq 0$): (c) shear stress, (d) density, (e) pressure.

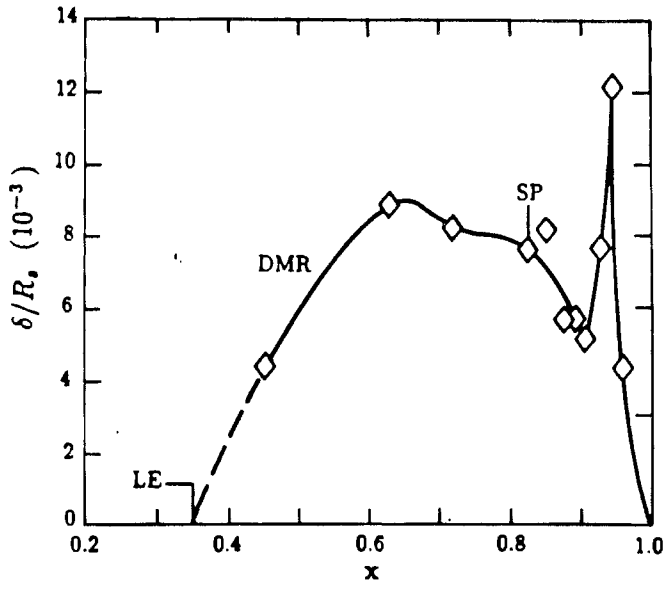

Fig. 16 Turbulent boundary layer thickness (δ/R_s) vs distance along the wedge ($x = r/R_s$).

form on the slip line at a distance from the triple point corresponding to a Reynolds number of about 10^5; then the flow rapidly becomes turbulent. The slip-line in the numerical simulation also rolled up into large-scale rotational structures. These structures were entrained in the free shear layer of the wall jet, and caused the boundary layer to roll up. Pairings of the structures in the two shear layers caused the boundary layer to separate at many locations, similar to the low-speed wall jet experiments.[18] This mixing transported material from above the shear layer all the way to the wall and mixed dust mass to the top of the jet.

The dimensions of the DMR shock structure grew linearly (i.e., self-similarly) with time. The dimensions of the wall jet grew along with the DMR structure; however, turbulence destroyed the coherence of the flow. This led to pulsations in the jet that sent acoustic waves toward the foot of the Mach stem.

Similarity coordinates ξ and η were used to sample the flow field over many turbulent cycles. Time averaging in these coordinates was used to find both the mean and rms profiles of the wall jet and boundary layer flow without resorting to turbulence modeling.

The calculations showed that there is no single boundary layer velocity profile in the DMR region; instead, the profiles depend on ξ because of gradients in the mean flow. They vary systematically from the clean $n = 1/7$ power function near the foot of the Mach stem to the DG dusty boundary layer profile near the moving stagnation point. Behind the DMR region, the profiles again approach the $n = 1/7$ power function profile.

The calculated boundary layer thickness grew to a peak value of $\delta/R_s \simeq 0.009$, at a distance well behind the DMR structure. No simple analytic relation could be found for the boundary layer height; rather, the calculated curve $\delta/R_s = f(x)$ in Fig. 16 is recommended. The turbulent mixing widths and the mean-flow profiles are probably accurate, but data are needed, especially to check the rms profiles.

In conclusion, we recommend a direct calculation of the turbulent mixing for such problems—because the dust mass modifies the turbulence and because of the complexity of the nonlinear interactions of the vortex structures in the wall jet. In other words, one should time-average the *solution*, not the equations. In the future, this approach should be used to calculate the turbulent mixing in nonsteady blast wave reflection problems.

References

[1]Colella, P., Ferguson, R.E., Glaz, H.M., and Kuhl, A.L., "Mach Reflection from an HE-Driven Blast Wave," *Dynamics of Explosions and Reactive Systems*, Progress in Astronautics and Aeronautics, Vol. 106, AIAA, 1986, pp. 388–421.

[2]Matsuo, K., Aoki, T., and Hirahara, H., "Visual Studies of Characteristics of Slip Stream in Mach Reflection of a Shock Wave," *Flow Visualization IV*, edited by C. Véret, Hemisphere, Washington, DC, 1988.

[3]Mach, E., "Über den Verlauf der Funkenwellen in der Ebene und im Raume," *Sitzungsber. Akad. Wiss. Wien*, Vol. 77, 1878, pp. 819–838.

[4]von Neumann, J. *Progress on the Theory of Shock Waves, National Defense Research Committee 8, Office of Scientific Research and Development* No. 1140, 1943.

[5]Polachek, H., and Seeger, R.J., "Shock Wave Interactions," *Fundamentals of Gas Dynamics: Vol. III of High Speed Aerodynamics and Jet Propulsion*, edited by H.W. Emmons, Princeton Univ. Press, Princeton, NJ, 1958.

[6]Courant, R., and Friedrichs, K.O., *Supersonic Flow and Shock Waves*, Interscience, New York, 1948.

[7]Smith, L.G., "Photographic Investigation of the Reflection of Plane Shocks in Air," USRD Rept. No. 6271, Underwater Sound Reference Detachment, U.S. Navy; or NORC Rep. No. A 2350, Naval Ordnance Research Center, U.S. Navy, 1945.

[8]White, D.R., "An Experimental Survey of the Mach Reflection of Shock Waves," Technical Rept. II-10, Department of Physics, Princeton Univ., Princeton, NJ, 1951.

[9]Bazhenova, T.V., Fokeev, V.P., and Gvozdeva, L.G., "Regions of Various Forms of Mach Reflection and its Transition to Regular Reflection," ACTA Astronautica, Vol. 3, 1976, pp. 131–140.

[10]Ben-Dor, G., and Glass, I.I., "Domains and Boundaries of Nonstationary Oblique-Shock-Wave Reflexions. 1. Diatomic Gas," *Journal of Fluid Mechanics*, Vol. 92, 1979, pp. 459–496.

[11]Glass, I.I., "Some Aspects of Shock Wave Research, *AIAA Journal*, Vol. 25, No. 2, 1987, pp. 214–229.

[12]Glaz, H.M., Colella, P., Glass, I.I., and Deschambault, R.L., "A Numerical Study of Oblique Shock-Wave Reflections with Experimental Comparisons," *Proceedings of the Royal Society of London, Ser. A*, Vol. 398, 1985, pp. 117–140.

[13]Glaz, H.M., Collela, P., and Glass, I.I., "A Detailed Numerical, Graphical and Experimental Study of Oblique Shock Wave Reflections," UTIAS Report No. 285, University of Toronto, Toronto, Canada, 1986.

[14]Glowacki, W.J., Kuhl, A.L., Glaz, H.M., and Ferguson, R.E., "Shock Wave Interaction with High Sound Speed Layers," *Proceedings of the 15th International Symposium on Shock Waves and Shock Tubes*, edited by D. Bershader and R. Hanson, Stanford Univ. Press, Palo Alto, CA, 1986.

[15]Kuhl, A.L., Chien, K.-Y., Ferguson, R.E., Collins, J.P., Glaz, H.M., and Colella, P., "Simulation of a Turbulent, Dusty Boundary Layer behind a Shock," *Current Topics in Shock Waves*, edited by Y. Kim, American Institute of Physics, New York, NY, 1990 (in press).

[16]Colella, P. and Glaz, H.M., "Efficient Solution Algorithms for the Riemann Problem for Real Gases," *Journal of Computational Physics*, Vol. 59, No. 2, 1985, pp. 264–289.

[17]Sedov, L.I., *Similarity and Dimensional Methods in Mechanics*, Academic Press, New York, 1959.

[18]Bajura, R.A., and Catalano, M.R., "Transition in a Two-Dimensional Plane Wall Jet," *Journal of Fluid Mechanics*, Vol. 70, 1975, pp. 773–799.

[19]Batt, R.G., Kulkarny, V.A., Behrens, H.W., and Rungaldier, H., "Shock-induced Boundary Layer Dust Lofting," *Shock Tubes and Waves*, edited by H. Grönig, VCH, Weinheim, FRG, 1988, pp. 1582–1589.

[20]Mirels, H., "Turbulent Boundary Layer Induced by a Thermal Precursor," Report SD-TR-86-38, Aerospace Corp., El Segundo, CA, 1986.

[21]Chien, K.-Y., Ferguson, R.E., Kuhl, A.L., Glaz, H.M., and Colella, P., "Inviscid Simulations of Turbulent Shear Layers: Fluctuating-Flow Profiles," *7th Symposium on Turbulent Shear Layers*, Stanford University, Palo Alto, CA (to be published).

Numerical Simulation of the Change in the Supersonic Flow Past a Body Produced by Switching on a Nearby Heat Source

T. V. Bazhenova, V. N. Lyakhov, and S. M. Kharitonov
USSR Academy of Sciences,
Moscow, USSR

Abstract

A heat source near a body around which a gas flows at a supersonic velocity may significantly change the gasdynamics parameters at the body surface. Numerical simulation is used to investigate the changes in parameters on the surface of a spherical body and the drag coefficient C when a heat source is placed on the symmetry axis in front of or behind the body.

Problem Formulation

As shown in Fig. 1, a spherical body of radius R_1 is initially placed in a supersonic gas flow whose parameters are R_1, ρ_1, U_1, and the Mach number M_1 Bow-shock wave SW_1 is situated at a distance δ in front of the body on the axis from the frontal point.

The pressure-drag coefficient is specified by

$$C = \frac{\int_\Sigma p_w \cos\theta d\sigma}{(\rho_1 U_1 F_1/2)} \tag{1}$$

when $d\sigma = R_1^2 \sin\theta d\theta d\varphi$ is an element of the body surface, p_w is the pressure on the body surface, $F_1 = \pi R_1^2$ is the area of the body midsection, and $\rho_1 U_1^2/2$ is the dynamic pressure of an unperturbed flow.

At time $t = t_s$ a heat source $a\,b$, whose power is Q_s (J/sec) and volume is V_s, is switched on at a distance Δ_s from the body surface. The flow near the body rearranges and a new stationary flow is established. The drag